

Research Article

Suppression of Switched Reluctance Motor Vibration of In-Wheel Motor Electric Vehicle

Funing Yang  and Yanyang Wang 

The Key Laboratory of Automotive Engineering, Xihua University, Chengdu 610039, China

Correspondence should be addressed to Yanyang Wang; yywang@mail.xhu.edu.cn

Received 18 May 2018; Revised 8 October 2018; Accepted 23 October 2018; Published 15 November 2018

Academic Editor: Manuel Pineda-Sanchez

Copyright © 2018 Funing Yang and Yanyang Wang. This is an open access article distributed under the Creative Commons Attribution License, which permits unrestricted use, distribution, and reproduction in any medium, provided the original work is properly cited.

Switched reluctance motor (SRM) has got great attention in in-wheel motor electric vehicle (IWM-EV), but SRM vertical force, the vertical component of SRM unbalanced radial force, yields SRM vertical vibration and does harm to dynamic performance of IWM-EV. In order to reduce the SRM vertical vibration, electromagnetic active suspension and a linear quadratic Gaussian (LQG) controller were used to suppress the unbalanced radial force in this paper. All the models and the controller were constructed in Matlab/Simulink R2015b. The controller considers five performance indexes: vehicle body acceleration, SRM airgap eccentricity, SRM stator acceleration, suspension dynamic deflections, and tyre deformation. Analytic Hierarchy Process (AHP) was used to calculate the weighted coefficients of performance indexes. Simulations indicate that this electromagnetic active suspension can reduce SRM vertical vibration obviously and improve dynamic performance of IWM-EV.

1. Introduction

Switched reluctance motor (SRM) has achieved good performance due to its remarkable advantages: high starting torque, wide operating speed range, and high efficiency. These advantages endow SRM with great potential on in-wheel motor electric vehicles (IWM-EV). However, asymmetrical magnetic pull caused by airgap eccentricity yields unbalanced radial force; this unbalanced radial force is recognized as one of the main reasons for the SRM vibration [1–5]. To reduce the vibration, scholars have focused on exploring the structure and control strategies of SRM [6–8].

On SRM structure, integrated design and the optimization of SRM components are main methods to reduce SRM vibration, such as multiobjective optimization design method [9], new stator tooth [10], new rotor tooth [11], and new poles ratio [12]. On SRM control strategies, varieties of methods have been proposed, such as torque distribution controller [13], multilevel systematic design method [14], and new motor torque controller [15]. The above studies do reduce the SRM vibration; however, these studies focus only on SRM itself; the negative influence of SRM on vehicle

dynamic performance has not been fully considered. As the main component that flexibly connects the wheel and the vehicle body, suspension transmits the force acting between the wheel and the vehicle body. As a kind of suspension system, electromagnetic active suspension can produce controllable active force, which enables the suspension system to dynamically adjust the supporting force according to the vibration of wheel and vehicle body. In the previous work, we analyzed the influence of the SRM unbalanced radial force on comfort and stability of IWM-EV. The conclusion [16, 17] shows SRM vertical force is highly coupled with road excitation and SRM airgap eccentricity, and this coupling yields SRM vertical vibration that does harm to comfort and stability. This study used electromagnetic active suspension and linear quadratic Gaussian (LQG) controller to reduce the SRM vertical vibration and the negative influence on vehicle dynamic performance.

In order to conduct this study, a full IWM-EV model, SRM vertical force model, and control diagram for the electromagnetic active suspension are built in Matlab/Simulink R2015b. Then the weighted coefficients are calculated and LQG controller is completed. Finally, the frequency responses

TABLE I: The SRM parameter values.

Definition	Symbol	Units	Value
Airgap	g	m	0.00025
Minimum inductance	L_q	H	0.0019
Maximum inductance	L_d	H	0.0318
Saturated inductance	L_{dsat}	H	0.0013
Maximum flux linkage	Ψ_m	Wb	0.9

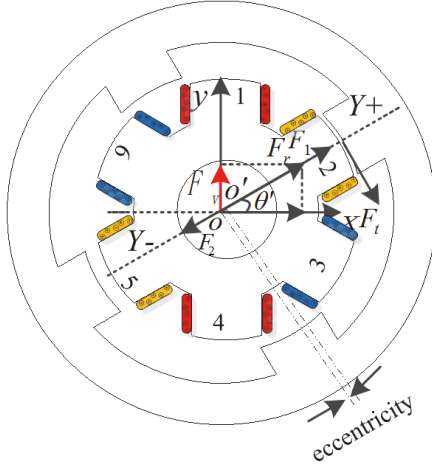


FIGURE 1: SRM vertical force.

on stochastic roads and time responses on representative roads are analyzed. Conclusion shows that the electromagnetic active suspension can effectively reduce SRM vibration and the negative influence on vehicle dynamic performance.

2. IWM-EV Modeling

Two models were constructed for studying the effects of electromagnetic active suspension. One is SRM vertical force model that reflects the SRM vertical force exerting on the wheel; another is full IWM-EV model that reflects the influence of electromagnetic active suspension force and unbalanced vertical force on vehicle.

2.1. SRM Vertical Force Model. Because of the geometrically balanced motor structure, the SRM radial force is always considered zero. But the vehicle load and road excitation [17] will yield SRM airgap eccentricity, due to which, the radial force is always not zero. In this study, The primary objective is to reduce the vertical vibration of SRM and the negative influence on vehicle dynamic performance, the well-known 6/4 outside-rotor SRM, like [18, 19], is shown in Figure 1. The SRM parameter values are listed in Table 1. According to [20], the difference magnetic pull between each pair of poles yields

the unbalanced radial force, and the radial force of opposite stator poles can be described as follows.

$$F_1 = -\frac{\sin(\theta_0)}{g_m - \Delta g} T = -\frac{r \sin(\theta_0)}{g_m - \Delta g} F_t \quad (1)$$

$$F_2 = -\frac{\sin(\theta_0)}{g_m + \Delta g} T = -\frac{r \sin(\theta_0)}{g_m + \Delta g} F_t \quad (2)$$

The unbalanced radial force is follows.

$$F_r = F_1 - F_2 \quad (3)$$

The vertical force that is the vertical component of the unbalanced radial force can be described as

$$F_v = F_r \sin(\theta') \quad (4)$$

where θ_0 is the overlap angle of stator and rotor, F_t is tyre tangential force, g_m is airgap length of SRM, Δg is the airgap eccentricity, and θ' is the angle between stator and wheel longitudinal axis. Each pair of opposite stator with eccentricity will yield unbalanced radial force, for the convenience of presentation, only stators 1 and 4 are picked out to investigate the influence of SRM vertical force on SRM vibration and vehicle dynamic performance. When the θ' is 90° , SRM unbalanced radial force is equal to SRM vertical force.

2.2. Vehicle Model. To simulate the effects of electromagnetic active suspension force on IWM-EV, the required vehicle dynamics model needs to reflect contributions of both electromagnetic active suspension force and SRM vertical force. A vehicle model which has been proved reasonably well in previous work [16, 17] is developed as shown in Figure 2, and the governing equations of the vehicle motions can be described as

$$M_t \ddot{x} = -(F_{xfl} + F_{xfr}) \cos \delta - (F_{yfl} + F_{yfr}) \sin \delta - F_{xrl} - F_{xrr} \quad (5)$$

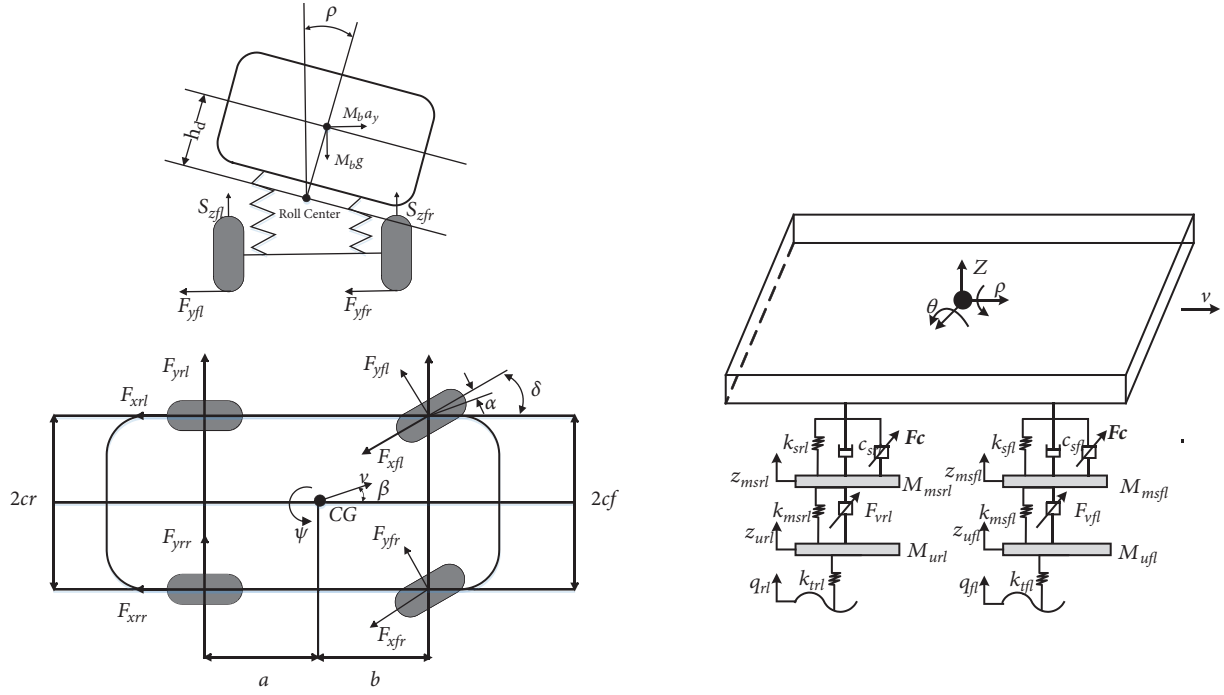


FIGURE 2: Schematic diagram of the vehicle model.

$$M_t \ddot{y} = -(F_{xfl} + F_{xfr}) \sin \delta + (F_{yfl} + F_{yfr}) \cos \delta + F_{yrl} + F_{yrr} \quad (6)$$

$$M_b \ddot{z} = S_{zfl} + S_{zfr} + S_{zrl} + S_{zrr} - F_{cfl} - F_{cfr} - F_{crl} - F_{crr} \quad (7)$$

$$I_x \ddot{\rho} = c_f (S_{zfl} - S_{zfr}) + c_r (S_{zrl} - S_{zrr}) + h_c [-(F_{xfl} + F_{xfr}) \sin \delta + (F_{yfl} + F_{yfr}) \cos \delta + F_{yrl} + F_{yrr}] + M_b g (h_{cg} - h_c) \sin \rho \quad (8)$$

$$I_y \ddot{\theta} = -a (S_{zfl} + S_{zfr}) + b (S_{zrl} + S_{zrr}) + h_p [(F_{xfl} + F_{xfr}) \cos \delta + (F_{yfl} + F_{yfr}) \sin \delta + F_{xrl} + F_{xrr}] + M_b g (h_{cg} - h_p) \sin \theta \quad (9)$$

$$I_z \ddot{\psi} = a [-(F_{xfl} + F_{xfr}) \sin \delta + (F_{yfl} + F_{yfr}) \cos \delta] - b (F_{yrl} + F_{yrr}) + c_f [(F_{xfl} - F_{xfr}) \cos \delta + (F_{yfl} - F_{yfr}) \sin \delta] + c_r (F_{xrl} - F_{xrr}) \quad (10)$$

where S_{zij} , the suspension vertical forces at each corner, is as follows.

$$S_{zfl} = -k_{sfl} (z + c_f \rho - a\theta - z_{msfl}) - c_{sfl} (\dot{z} + c_f \dot{\rho} - a\dot{\theta} - \dot{z}_{msfl})$$

$$\begin{aligned} S_{zfr} &= -k_{sfr} (z - c_f \rho - a\theta - z_{msfr}) - c_{sfr} (\dot{z} - c_f \dot{\rho} - a\dot{\theta} - \dot{z}_{msfr}) \\ S_{zrl} &= -k_{srl} (z + c_r \rho + b\theta - z_{msrl}) - c_{srl} (\dot{z} + c_r \dot{\rho} + b\dot{\theta} - \dot{z}_{msrl}) \\ S_{zrr} &= -k_{srr} (z - c_r \rho + b\theta - z_{msrr}) - c_{srr} (\dot{z} - c_r \dot{\rho} + b\dot{\theta} - \dot{z}_{msrr}) \end{aligned} \quad (11)$$

Equations of the vertical motion of the aggregate mass of the tyres, the rims, and the SRM rotors at each corner are as follows.

$$\begin{aligned} M_{ufll} \ddot{z}_{ufll} &= k_{msfl} (z_{msfl} - z_{ufll}) - k_{tfl} (z_{ufll} - q_{fl}) - F_{vfl} \\ M_{ufr} \ddot{z}_{ufr} &= k_{msfr} (z_{msfr} - z_{ufr}) - k_{tfr} (z_{ufr} - q_{fr}) - F_{vfr} \\ M_{urrl} \ddot{z}_{urrl} &= k_{msrl} (z_{msrl} - z_{urrl}) - k_{trl} (z_{urrl} - q_{rl}) - F_{vrl} \\ M_{urrr} \ddot{z}_{urrr} &= k_{msrr} (z_{msrr} - z_{urrr}) - k_{trr} (z_{urrr} - q_{rr}) - F_{vrr} \end{aligned} \quad (12)$$

Equations of the vertical motion of the aggregate mass of the SRM stator and housing are

$$M_{msfl} \ddot{z}_{msfl} = k_{sfl} (z + c_f \rho - a\theta - z_{msfl}) + c_{sfl} (\dot{z} + c_f \dot{\rho} - a\dot{\theta} - \dot{z}_{msfl})$$

TABLE 2: The vehicle parameter values.

Definition	Symbol	Units	Value
Vehicle total mass	M_t	kg	1770
Sprung mass	M_b	kg	1350
Mass of tyre, rim and SRM rotor of front wheel	M_{ufj}	kg	70
Mass of tyre, rim and SRM rotor of rear wheel	M_{urj}	kg	65
Mass of SRM stator and housing	M_{msij}	kg	37.5
Roll moment of inertia	I_x	Kg m ²	480
Pitch moment of inertia	I_y	Kg m ²	1895
Yaw moment of inertia	I_z	Kg m ²	1875
Height of CG	h_{cg}	m	0.504
Height of pitch center	h_p	m	0.4
Height of roll center	h_c	m	0.25
Distance from CG to front axle	a	m	1.08
Distance from CG to rear axle	b	m	1.62
Track width of front axle	c_f	m	1.4
Track width of rear axle	c_r	m	1.385
Wheel inertia	I_{wi}	Kg m ²	1.8
Effective radius of wheel	R	m	0.269
Stiffness of front suspension	k_{sfj}	N/m	22500
Stiffness of rear suspension	k_{srj}	N/m	19600
Damping of front/rear suspension	c_{sij}	Ns/m	1695
Sum of SRM and hub bearing stiffness	k_{msij}	N/m	6500000
Stiffness of tyre	k_{tij}	N/m	150000

$$\begin{aligned}
& -k_{msfl}(z_{msfl} - z_{ufl}) + Fv_{fl} + Fc_{fl} \\
M_{msfr}\ddot{z}_{msfr} &= k_{sfr}(z - c_f\rho - a\theta - z_{msfr}) \\
& + c_{sfr}(z - c_f\rho - a\theta - z_{msfr}) \\
& - k_{msfr}(z_{msfr} - z_{ufr}) + Fv_{fr} + Fc_{fr} \\
M_{msrl}\ddot{z}_{msrl} &= k_{srl}(z + c_r\rho + b\theta - z_{msrl}) \\
& + c_{srl}(z + c_r\rho + b\theta - z_{msrl}) \\
& - k_{msrl}(z_{msrl} - z_{url}) + Fv_{rl} + Fc_{rl} \\
M_{msrr}\ddot{z}_{msrr} &= k_{srr}(z - c_r\rho + b\theta - z_{msrr}) \\
& + c_{srr}(z - c_r\rho + b\theta - z_{msrr}) \\
& - k_{msrr}(z_{msrr} - z_{urr}) + Fv_{rr} + Fc_{rr}
\end{aligned} \tag{13}$$

where x , y , and z are the longitudinal displacement, the lateral displacement, and the vertical displacement, respectively, of the sprung mass of the vehicle; ρ , θ , and ψ are the vertical, pitch, and roll motion of the sprung mass of the vehicle; δ is the steering angle; F_c is the electromagnetic active suspension force; F_{xij} and F_{yij} are the longitudinal tyre force and the lateral tyre force at each wheel; q_{ij} is road displacement excitation at each wheel; Fv_{ij} is the unbalanced vertical force of each SRM; M_{msij} is the aggregate mass of tyre, hub, and SRM rotor; M_{uij} is the aggregate mass of SRM stator and housing; and k_{msij} is the bearing stiffness. The subscripts i

in the equations refer to the front (f) or rear (r), and the subscripts j in the equations refers to the left (l) side or the right (r) side. The vehicle parameter values used for this study are listed in Table 2.

The Pacejka nonlinear tyre model [21] is adopted in this paper to simulate the nonlinearity tyre force. The equations of the Pacejka nonlinear tyre mode are

$$\begin{aligned}
F_{xij}(\lambda) &= D_x \\
& \cdot \sin\left(C_x \arctan\left\{B_y\lambda - E_x[B_x\lambda - \arctan(B_x\lambda)]\right\}\right)
\end{aligned} \tag{14}$$

$$\begin{aligned}
F_{yij}(\alpha) &= D_y \\
& \cdot \sin\left(C_y \arctan\left\{B_y\alpha - E_y[B_x\alpha - \arctan(B_x\alpha)]\right\}\right)
\end{aligned} \tag{15}$$

$$B_x = \frac{a_3 \sin[2 \arctan(F_z/a_4)]}{C_x D_x}$$

$$C_x = b_0$$

$$D_x = \frac{a_1 F_z^2 + a_2 F_z}{1000}$$

$$E_x = a_5 F_z + a_6$$

$$B_y = \frac{b_3 \sin[2 \arctan(F_z/b_4)]}{C_y D_y}$$

$$C_y = b_0$$

$$D_y = \frac{b_1 F_z^2 + b_2 F_z}{1000}$$

$$E_y = b_5 F_z + b_6 \quad (16)$$

where λ is the slip ratio and $B_x, C_x, D_x, E_x, B_y, C_y, D_y,$ and E_y are empirical parameters. F_{xij}, F_{yij} are the longitudinal force and lateral force.

3. LQG Controller of Electromagnetic Active Suspension

In this paper, several performance indexes of IWM-EV are considered by linear quadratic Gaussian (LQG) controller, such as vehicle body acceleration, airgap eccentricity, SRM stator acceleration, suspension dynamic deflections, and tyre

deformation. It is easy to use the methodology of Analytic Hierarchy Process (AHP) to select the weighted coefficients of performance indexes [22]. This LQG controller is based on optimal control theory and the controller can propose different objective functions according to design requirements and improve the vehicle performance by comprehensively considering various performance indexes.

3.1. State Equation. 24 state variables and 14 output variables are chosen to constitute the vehicle system for controller, and the state equation can be described as

$$\dot{X} = AX + Bu + GQ \quad (17)$$

$$Y = CX + Du \quad (18)$$

where

$$X = [\dot{z} \ \theta \ z \ \dot{z}_{msfl} \ \dot{z}_{msfr} \ \dot{z}_{msrl} \ \dot{z}_{msrr} \ z_{msfl} \ z_{msfr} \ z_{msrl} \ z_{msrr} \ \dot{z}_{ufl} \ \dot{z}_{ufr} \ \dot{z}_{url} \ \dot{z}_{urr} \ z_{ufl} \ z_{ufr} \ z_{url} \ z_{urr} \ q_{fl} \ q_{fr} \ q_{rl} \ q_{rr}]^T \quad (19)$$

$$Y = [z \ \theta \ Z_{msfl} \ Z_{msfr} \ Z_{msrl} \ Z_{msrr} \ Z_{ufl} \ Z_{ufr} \ Z_{url} \ Z_{urr} \ q_{fl} \ q_{fr} \ q_{rl} \ q_{rr}]^T \quad (20)$$

$$u = F_c \quad (21)$$

where X is the state variables, Y is the output variables, u is the control vector, and A is the system matrix. B is control matrix. G is disturbance matrix. C is the output matrix. D is transfer matrix.

3.2. Selection of Performance Indexes' Weighted Coefficients for LQG Controller. AHP is a decision-making method. It decomposes elements that are always related to decision-making into objectives, criteria, and programs and then makes qualitative and quantitative analysis on this basis. It was used to select weighted coefficients of performance indexes for LQG controller [23].

3.2.1. Quantitating Scale Factor. The root mean square (RMS) of dynamic characteristics of the passive suspension vehicle can be produced by simulating the passive suspension vehicle model under the corresponding conditions. According to the literature, [22, 23], scale factors of vehicle dynamic characteristics can be described by the following equations:

$$\sigma_{BA}^2 \times 1 = \sigma_{PA}^2 \times \beta_{PA} = \sigma_{AEij}^2 \times \beta_{AEij} = \sigma_{TDij}^2 \times \beta_{TDij}$$

$$= \sigma_{SDDij}^2 \times \beta_{SDDij} \quad (22)$$

where $\sigma_{BA}, \sigma_{PA}, \sigma_{AEij}, \sigma_{TDij}, \sigma_{SDDij}$ are RMS of vehicle body vertical acceleration (BVA), pitch angle (PA), airgap eccentricity (AE), tyre deformation (TD), and suspension dynamic deflections (SDD). $\beta_{PA}, \beta_{AEij}, \beta_{TDij}, \beta_{SDDij}$ are pitch angle scale factor, airgap eccentricity scale factor, tyre deformation scale factor, and suspension dynamic deflections scale factor; vehicle body vertical acceleration (BVA) scale factor is 1.

3.2.2. Subjective Weighted Coefficient

(1) Making Judgment Matrix H . h_{ij} (no unit) is the relative importance ratio of the index i and j . Table 3 is a comparison table of the relative importance of each index. According to Table 3, judgment matrix H shown in (23) can be constructed.

$$H = (h_{ij})_{n \times n} = \begin{bmatrix} 1 & h_{12} & h_{13} & \cdots & \cdots & h_{1n} \\ \frac{1}{h_{12}} & 1 & h_{23} & h_{24} & \cdots & h_{2n} \\ \frac{1}{h_{13}} & \frac{1}{h_{23}} & 1 & h_{34} & \cdots & h_{3n} \\ \vdots & \frac{1}{h_{24}} & \frac{1}{h_{34}} & \cdots & \cdots & \cdots \\ \vdots & \vdots & \vdots & & & \vdots \\ \frac{1}{h_{1n}} & \frac{1}{h_{2n}} & \frac{1}{h_{3n}} & \cdots & \cdots & 1 \end{bmatrix} \quad (23)$$

Calculate multiplying vector of every row.

$$M = [M_1, M_2, M_3, \dots, M_n]^T$$

$$M_i = \prod_{j=1}^n h_{ij}, \quad (i, j = 1, 2, 3, \dots, n) \quad (24)$$

TABLE 3: Comparison table.

i/j	Equal	Moderately	Strongly	Very	Extremely
h_{ij}	1	3	5	7	9

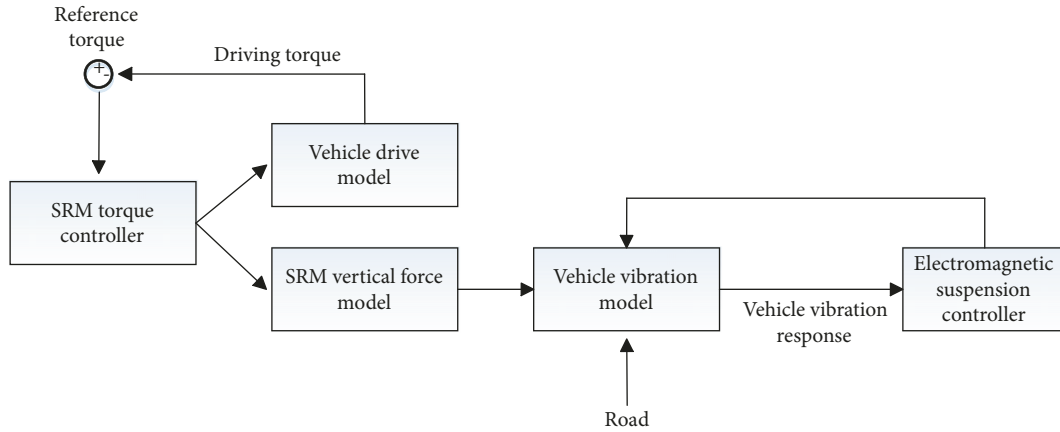


FIGURE 3: Control diagram for the electromagnetic active suspension.

Calculate $\sqrt[n]{\bar{W}}$ and W

$$\begin{aligned}\bar{W} &= [\bar{W}_1, \bar{W}_2, \bar{W}_3, \dots, \bar{W}_n]^T \\ \bar{W}_i &= \sqrt[n]{M_i}, \quad (i = 1, 2, 3, \dots, n) \\ W &= \frac{\bar{W}}{\sum_{i=1}^n \bar{W}_i}, \quad (i = 1, 2, 3, \dots, n)\end{aligned}\quad (25)$$

where W is the subjective weighted coefficient.

(2) *Maximum Eigenvalue and Consistency Checking of Matrix H*

$$\lambda_{\max} = \sum_{i=1}^n \frac{(HW)_i}{nW_i}, \quad (i = 1, 2, 3, \dots, n) \quad (26)$$

where λ_{\max} is the maximum eigenvalue of H .

If every element in matrix H satisfies the equations $h_{ij} = 1/h_{ji}$ and $h_{ij} = h_{ik} \times h_{kj}$, the matrix H is the consistency matrix. The method of consistency checking is comparing random consistency ratio CR .

$$CR = \frac{\lambda_{\max} - n}{RI(n-1)}, \quad (i = 1, 2, 3, \dots, n) \quad (27)$$

RI is the random consistency index. When n is 14, RI is 1.59. If CR is less than 1, H passes the consistency checking. If CR is more than 1, H needs to be revised [24].

3.2.3. *Weighted Coefficients.* Subjective weighted coefficients of pitch angle, airgap eccentricity, tyre deformation, and suspension dynamic deflections can be calculated as follows.

$$W_i = \frac{W_i}{\gamma_i} \quad (28)$$

$$q_1 = 1,$$

$$q_2 = \beta_{PA} \gamma_2,$$

$$q_3 = \beta_{AEfl} \gamma_3,$$

$$q_4 = \beta_{AEfr} \gamma_4,$$

$$q_5 = \beta_{AErl} \gamma_5,$$

$$q_6 = \beta_{AErr} \gamma_6,$$

$$q_7 = \beta_{TDfl} \gamma_7,$$

$$q_8 = \beta_{TDfr} \gamma_8,$$

$$q_9 = \beta_{TDrl} \gamma_9,$$

$$q_{10} = \beta_{TDrr} \gamma_{10},$$

$$q_{11} = \beta_{SDDfl} \gamma_{11}$$

$$q_{12} = \beta_{SDDfr} \gamma_{12},$$

$$q_{13} = \beta_{SDDrl} \gamma_{13},$$

$$q_{14} = \beta_{SDDrr} \gamma_{14}$$

3.3. *LQG Controller Design.* The control diagram for the electromagnetic active suspension is shown in Figure 3. Vehicle body acceleration and pitch angle are chosen to be the performance indexes for improving ride comfort and handling stability. Airgap eccentricity, tyre deformation, and

suspension dynamic deflections of each wheel are chosen to be the performance indexes for reducing the vertical vibration of SRM.

The performance function is defined as follows:

$$\begin{aligned}
J = & \frac{1}{2} \int_0^{\infty} q_1 \ddot{z}_b^2 + q_2 \theta^2 + q_3 (z_{msfl} - z_{ufl})^2 \\
& + q_4 (z_{msfr} - z_{ufr})^2 + q_5 (z_{msrl} - z_{url})^2 \\
& + q_6 (z_{msrr} - z_{urr})^2 + q_7 (z_{ufl} - q_{fl})^2 \\
& + q_8 (z_{ufr} - q_{fr})^2 + q_9 (z_{url} - q_{rl})^2 \\
& + q_{10} (z_{urr} - q_{rr}) + q_{11} (z + c_f \rho - a\theta - z_{msfl})^2 \\
& + q_{12} (z - c_f \rho - a\theta - z_{msfr})^2 \\
& + q_{13} (z + c_r \rho - a\theta - z_{msrl})^2 \\
& + q_{14} (z + c_r \rho - a\theta - z_{msrr})^2 + Ru^2] dt = \frac{1}{2} \\
& \cdot \int_0^{\infty} Y^T Q Y + u^T R u) dt
\end{aligned} \quad (30)$$

where q_1 is the weighted coefficient of body vertical acceleration; q_2 is the weighted coefficient of pitch angle; $q_3, q_4, q_5,$ and q_6 are the weighted coefficients of airgap eccentricity; $q_7, q_8, q_9,$ and q_{10} are the weighted coefficients of tyre deformation; $q_{11}, q_{12}, q_{13},$ and q_{14} are the weighted coefficients of suspension dynamic deflections; Q is the weight matrix of the state; u is the control vector of F_c ; and R is the weighted coefficient of u .

Rewrite (30) as a standard form:

$$J = \frac{1}{2} \int_0^{\infty} [X^T Q' X + 2X^T N u + u^T R' u] dt \quad (31)$$

where

$$\begin{aligned}
Q' &= C^T Q C, \\
N &= C^T Q D, \\
R' &= R + D^T Q D \\
u &= -KX
\end{aligned} \quad (32)$$

$$u = -KX \quad (33)$$

and the optimal control feedback matrix K can be given by the Riccati equation.

$$\begin{aligned}
PA + A^T P + Q - (PB + N) R^{-1} (B^T P + N^T) &= 0 \\
K &= B^T P + N^T
\end{aligned} \quad (34)$$

It is easy to calculate feedback matrix K by using Matlab function as follows.

$$[K, S, E] = \text{lqr}(A, B, Q, R, N) \quad (35)$$

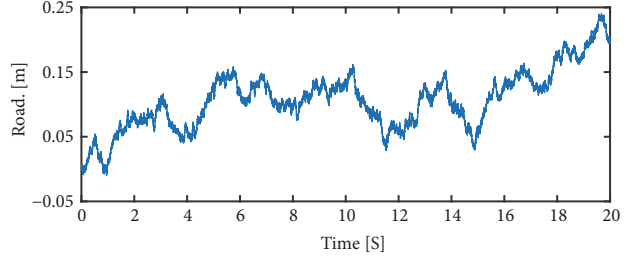


FIGURE 4: Effective road excitation.

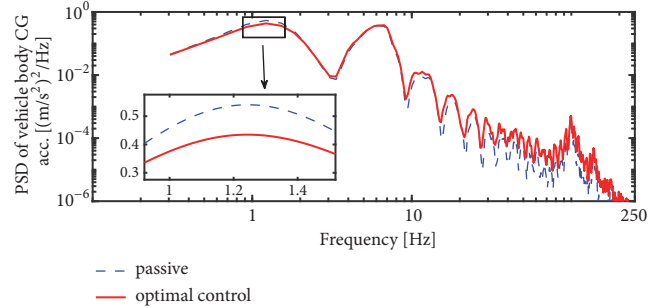


FIGURE 5: Frequency response of vehicle body acceleration.

4. Suppression of SRM Vertical Force and Promotion of Vehicle Dynamic Performance

SRM vibration and IWM-EV body movement influence each other, so it is difficult to improve the dynamic performance of the vehicle considering only the SRM structure and controller design. Therefore, this study used electromagnetic active suspension, connecting body and wheels, to reduce the SRM vibration and the negative influence on vehicle body.

4.1. Frequency Response on Stochastic Roads. For this simulation, the road excitations at four tyres are assumed to be the same, only the front left in-wheel SRM response is presented in this paper. In order to study the effects of electromagnetic active suspension under urban condition and high-speed condition, vehicle responses are simulated at 60 km/h vehicle speed on class C road and 100 km/h vehicle speed on class C road.

4.1.1. Response under Urban Condition. Vehicle responses are simulated at 60 km/h vehicle speed on class C road as shown in Figure 4.

Responses of vehicle body acceleration, airgap eccentricity, SRM stator acceleration, suspension dynamic deflections, and tyre deformation at 60 km/h are shown in Figures 5–9.

It can be seen that the electromagnetic active suspension can reduce the power spectral density (PSD) values of vehicle body acceleration, airgap eccentricity, SRM stator acceleration, suspension dynamic deflections, and tyre deformation at their resonance frequency. Specifically, Figure 5 shows that the resonance frequency of vehicle body acceleration is 1.221 Hz, and the peak value of vehicle body acceleration decreases from $0.5395 \text{ (m/s}^2\text{)}^2/\text{Hz}$ to $0.4343 \text{ (m/s}^2\text{)}^2/\text{Hz}$ and

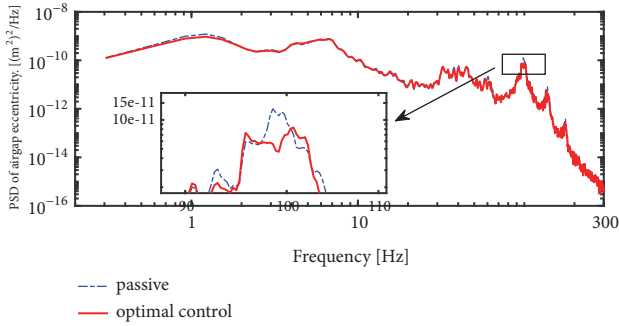


FIGURE 6: Frequency response of airgap eccentricity.

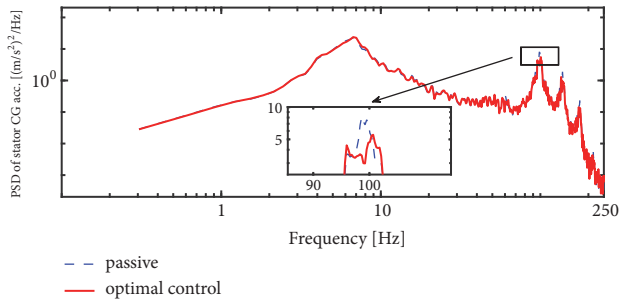


FIGURE 7: Frequency response of stator acceleration.

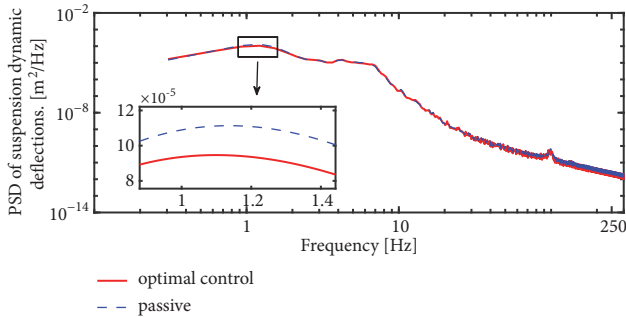


FIGURE 8: Frequency response of suspension dynamic deflections.

reduced by 19.5%. This indicates that the electromagnetic active suspension can reduce the force acting between the wheel and the vehicle body, and ride comfort improved. Figure 6 shows that the resonance frequency of airgap eccentricity is 98.57 Hz, and the peak value of airgap eccentricity decreases from $1.307e^{-10} \text{ m}^2/\text{Hz}$ to $8.339e^{-11} \text{ m}^2/\text{Hz}$ and reduced by 36.2%. Figure 7 shows that the resonance frequency of stator acceleration is 98.57 Hz, and the peak value of stator acceleration decreases from $8.147 \text{ (m/s}^2\text{)}^2/\text{Hz}$ to $5.520 \text{ (m/s}^2\text{)}^2/\text{Hz}$ and reduced by 32.2%. Figures 6 and 7 mean that electromagnetic active suspension conspicuously suppressed SRM vertical vibration, and operating stability of SRM improved. Furthermore, SRM's negative influence on the vehicle reduced. Figure 8 shows that the resonance frequency of suspension dynamic deflections is 1.221 Hz, and the peak value of suspension dynamic deflections decreases from $1.30e^{-4} \text{ m}^2/\text{Hz}$ to $1.06e^{-4} \text{ m}^2/\text{Hz}$ and reduced by 18.4%.

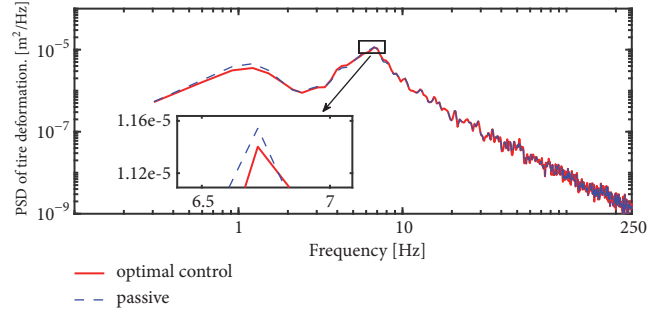


FIGURE 9: Frequency response of tyre deformation.

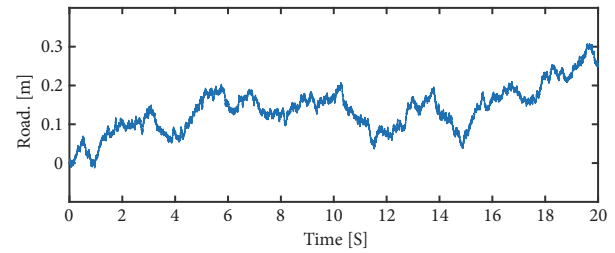


FIGURE 10: Effective road excitation.

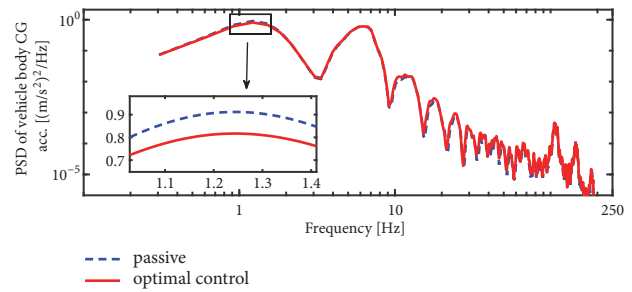


FIGURE 11: Frequency response of vehicle body acceleration.

Figure 9 shows that the resonance frequency of tyre deformation is 6.714 Hz, and the peak value of tyre deformation decreases from $1.154e^{-5} \text{ m}^2/\text{Hz}$ to $1.140e^{-5} \text{ m}^2/\text{Hz}$ and reduced by 1.21%. Because driving stability is related to suspension dynamic deflections and tyre deformation, decrease of them implies that electromagnetic active suspension can improve vehicle safety. Therefore, compared with passive suspension, electromagnetic active suspension can availablely reduce values of body acceleration, airgap eccentricity, SRM stator acceleration, and so on. Ride comfort and safety under urban condition improved.

4.1.2. Response under High-Speed Condition. Vehicle responses are simulated at 100 km/h vehicle speed on class C road as shown in Figure 10. Vehicle body acceleration, airgap eccentricity, SRM stator acceleration, tyre deformation, and suspension dynamic deflections responses at 100 km/h are shown in Figures 11–15.

Under high-speed condition, the power spectral density (PSD) values of vehicle body acceleration, airgap eccentricity,

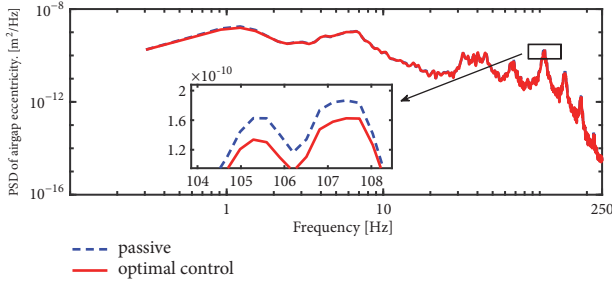


FIGURE 12: Frequency response of airgap eccentricity.

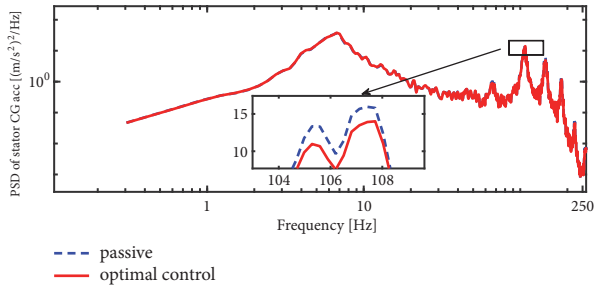


FIGURE 13: Frequency response of stator acceleration.

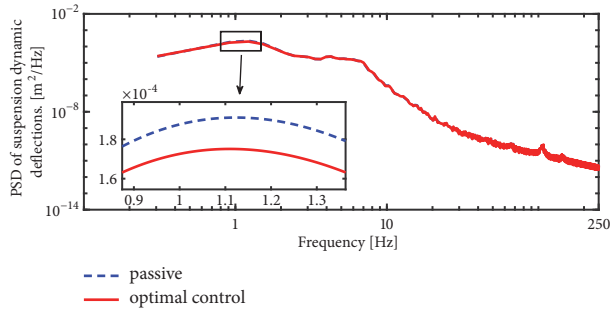


FIGURE 14: Frequency response of suspension dynamic deflections.

SRM stator acceleration, suspension dynamic deflections, and tyre deformation can be reduced at their resonance frequency. Figure 11 shows that the peak value of vehicle body acceleration decreases from $0.9104 (m/s^2)^2/Hz$ to $0.8158 (m/s^2)^2/Hz$ and reduced by 10.4%. This means that, even under high-speed conditions, the electromagnetic active suspension can still significantly reduce the vibration of the vehicle body, and the ride comfort improved obviously. As can be seen from Figures 12 and 13, the peak value of airgap eccentricity decreases from $1.867e^{-10} m^2/Hz$ to $1.625e^{-10} m^2/Hz$ and reduced by 13.0%; the peak value of stator acceleration decreases from $15.95 (m/s^2)^2/Hz$ to $13.91 (m/s^2)^2/Hz$ and reduced by 12.8%. This indicates that the vibration of SRM under high-speed condition was reduced effectively. Figure 14 shows that the peak value of suspension dynamic deflections decreases from $2.24e^{-4} m^2/Hz$ to $2.02e^{-4} m^2/Hz$ and reduced by 9.8%. Figure 15 shows that the peak value of tyre deformation decreases from $1.902e^{-5} m^2/Hz$ to $1.894e^{-5} m^2/Hz$ and reduced by 0.42%.

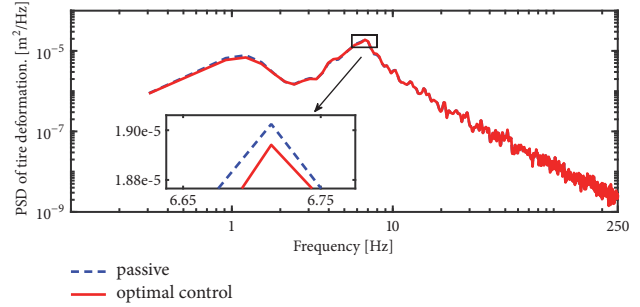


FIGURE 15: Frequency response of tyre deformation.

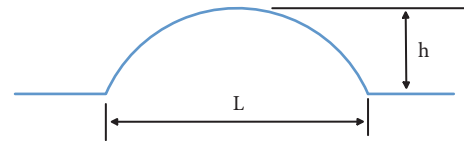


FIGURE 16: Bump road model.

Therefore, electromagnetic active suspension can improve ride comfort and reduce SRM vibration under high-speed condition. Because decreases of suspension dynamic deflections and tyre deformation can greatly enhance the driving stability under high-speed condition, the vehicle safety improved.

The effects of electromagnetic active suspension under high-speed condition are weaker than effects under urban condition, because the weighted coefficients of LQG controller are more suitable for urban condition. All the vehicle responses at both 60 km/h and 100 km/h were shown in Table 4.

4.2. Time Response on Representative Roads

4.2.1. Response on Bump Road. In order to simulate the speed bump, bump road model is shown in Figure 16. The simplified model can be described as (36), where L, h are the width and height of the bump and V is the vehicle speed. Setting different vehicle speed or changing the width of the bump can easily adjust road excitation frequency. To simulate the ordinary low frequency speed hump excitation, $L=0.8m$, $h=0.07m$, and V is $0.8 m/s$. Vehicle body acceleration, pitch angle, airgap eccentricity, suspension dynamic deflections, and tyre deformation responses on class C road are shown in Figures 17–21.

Figure 17 shows the vehicle body acceleration responses. When $t=1s$, the vehicle body starts to vibrate under the excitation of bump road. When $t=2.16s$, the vehicle body acceleration reaches peak value, and the peak value decreases by 6.11%. Figure 18 shows the response of pitch angle. When $t=1s$, the bump road excitation starts to affect the vehicle. When $t=3s$, the vehicle system tends to be stable. The peak value of pitch angle decreases by 3.16%. Figures 17 and 18 mean that the vertical vibration of the body was reduced and the ride comfort improved, because the vertical motion of the unsprung mass and its impact on vehicle body were reduced.

TABLE 4: Vehicle responses.

Frequency response	Resonance frequency (Hz)	Units	60 km/h			100 km/h		
			Passive	Optimal control	reduce by	Passive	Optimal control	reduce by
Vehicle body acceleration	1.221	$(m/s^2)^2/Hz$	0.5395	0.4343	19.5%	0.9104	0.8158	10.4%
Airgap eccentricity	98.57	m^2/Hz	$1.307e^{-10}$	$8.339e^{-11}$	36.2%	$1.867e^{-10}$	$1.625e^{-10}$	13.0%
Stator acceleration	98.57	$(m/s^2)^2/Hz$	8.147	5.520	32.2%	15.95	13.91	12.8%
Suspension dynamic deflections	1.221	m^2/Hz	$1.30e^{-4}$	$1.06e^{-4}$	18.4%	$2.24e^{-4}$	$2.02e^{-4}$	9.8%
Tyre deformation	6.714	m^2/Hz	$1.154e^{-5}$	$1.140e^{-5}$	1.21%	$1.902e^{-5}$	$1.894e^{-5}$	0.42%

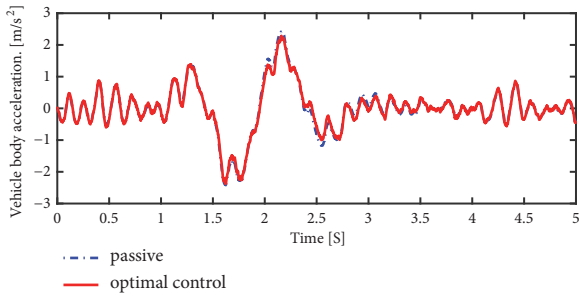


FIGURE 17: Time history response of vehicle body acceleration.

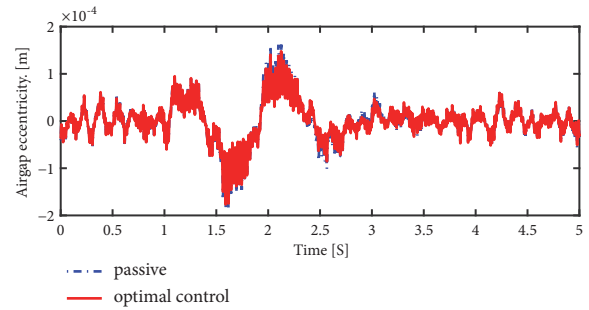


FIGURE 19: Time history response of airgap eccentricity.

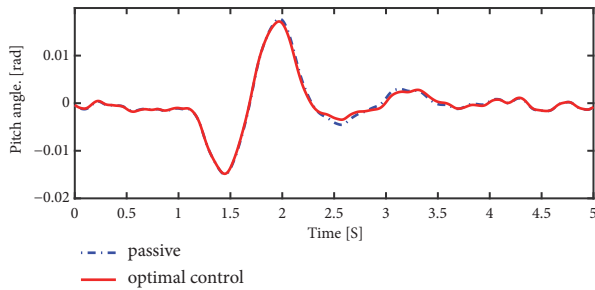


FIGURE 18: Time history response of pitch angle.

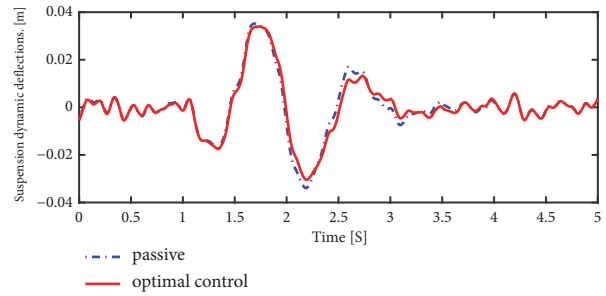


FIGURE 20: Time history response of suspension dynamic deflections.

As can be seen from Figures 19 and 20, the trend of airgap eccentricity is similar to vehicle body acceleration, and the peak value of airgap eccentricity decreases by 8.89%. When $t=1s$, the suspension system starts to shrink. When $t=3s$, the electromagnetic active suspension system approaches steady state that is faster than passive suspension system at $t=3.7s$. The peak value of suspension dynamic deflection decreases by 3.64%. Figure 21 shows that the peak value of tyre deformation decreases by 7.44%. This implies that the electromagnetic active suspension can effectively reduce the airgap eccentricity, suspension dynamic deflection, and tyre deformation on bump road. The unsprung mass had less

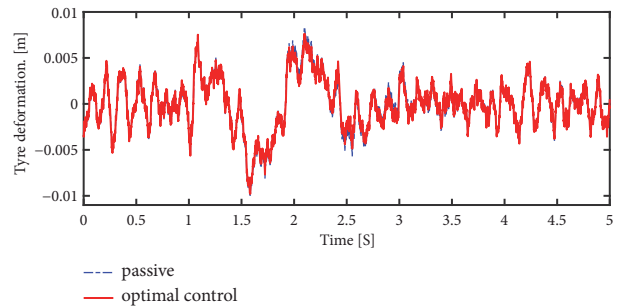


FIGURE 21: Time history response of tyre deformation.

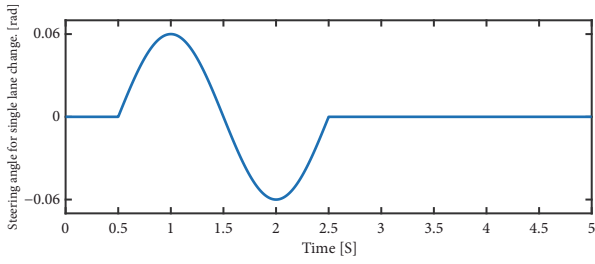


FIGURE 22: Single lane change.

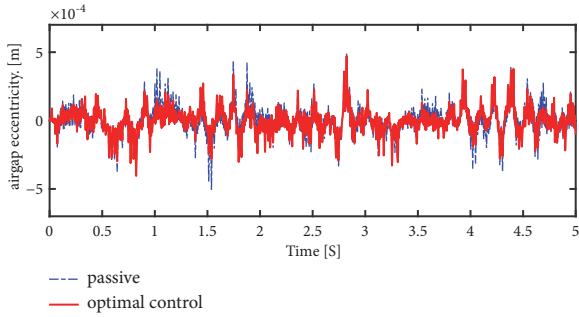


FIGURE 23: Time history response of airgap eccentricity.

influence on the body and can provide higher stability for the vehicle.

$$z_r = \frac{h(1 - \cos 2\pi ft)}{2r} \tag{36}$$

$$f = \frac{V}{L}$$

4.2.2. *Response on Single Lane Change.* In order to study the effects of electromagnetic active suspension on handling stability, vehicle responses are simulated under single lane change condition. The steering angle model is shown in Figure 22. Airgap eccentricity, roll angle, sideslip angle, and yaw rate responses at 100 km/h on class C road are shown in Figures 23–26.

Figure 23 shows that the airgap eccentricity response does not have much relevance to steering angle, but the electromagnetic active suspension efficiently reduces the airgap eccentricity. Figure 24 shows that the vehicle starts to roll at 0.5s. The roll angle reaches peak value at 1.8s and decreases by 3.66%. Figures 25 and 26 show that the trends of sideslip angle and yaw rate are similar to steering angle. Although the contributions of the electromagnetic active suspension to sideslip angle and yaw rate under this condition are not very significant, the electromagnetic active suspension system does have positive influences on the lateral dynamic performance.

5. Conclusions

In order to reduce SRM vertical vibration and improve IWM-EV dynamic performance, this paper used electromagnetic active suspension and LQG controller to suppress the SRM

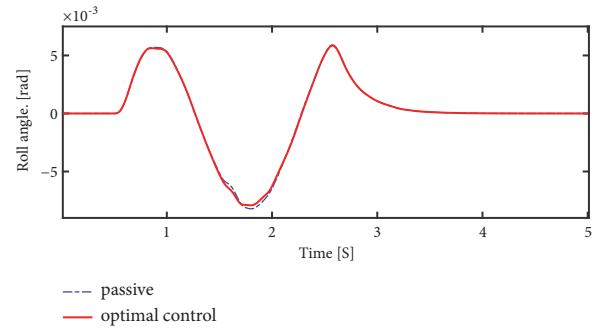


FIGURE 24: Time history response of roll angle.

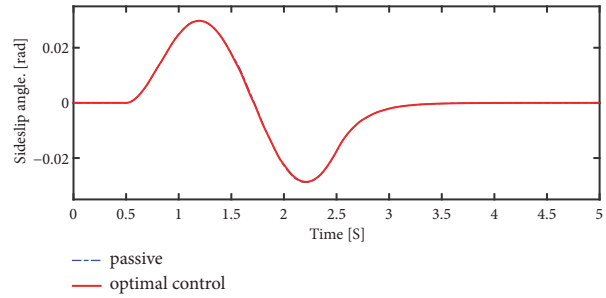


FIGURE 25: Sideslip angle.

unbalanced radial force. The controller based on optimal control theory can efficiently match electromagnetic active suspension. In theory, compared with the passive suspension, this electromagnetic active suspension can reduce SRM vertical vibration and provide better dynamic performance to the IWM-VE. Based on the analyzed simulation results, the following 3 conclusions can be summarize:

(1) This electromagnetic active suspension could effectively improve the ride comfort. Vehicle body acceleration was reduced on urban condition, high-speed condition, and representative roads. For urban condition, the vehicle body acceleration reduced by 19.5% near the vehicle body's resonance frequency 1.22 Hz. For high-speed condition, the vehicle body acceleration reduced by 10.4% near the vehicle body's resonance frequency 1.22 Hz.

(2) This electromagnetic active suspension could effectively reduce the SRM vertical vibration. SRM airgap eccentricity and stator acceleration were both reduced. Specifically, when the frequencies of the SRM airgap eccentricity and stator acceleration are near the stator's resonance frequency of 107.4 Hz, the SRM vertical vibration shows a most obvious drop.

(3) This electromagnetic active suspension could improve the safety. Under both urban condition and high-speed condition, suspension dynamic deflection and tyre deformation were reduced. On representative roads, electromagnetic active suspension reduced roll angle, sideslip angle, and yaw rate. It indicated that the electromagnetic active suspension can improve lateral dynamic performance and reduce SRM vertical vibration at the same time.

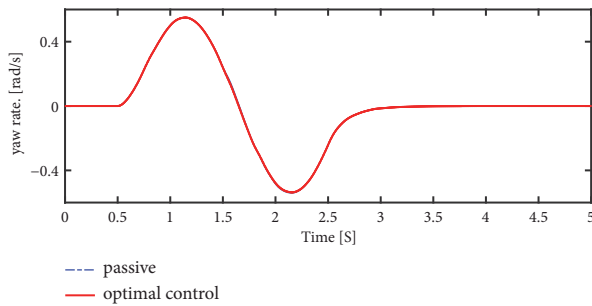


FIGURE 26: Yaw rate.

In summary, this paper used electromagnetic active suspension and LQG controller to effectively improve the IWM-EV ride comfort and safety and also reduce the SRM vertical vibration. Due to limited research resource, this paper does not construct an experimental platform to verify the simulation results. But we are preparing an experimental platform and will give introduction in the next work.

Data Availability

The data used to support the findings of this study are available from the corresponding author upon request.

Conflicts of Interest

The authors declare that they have no conflicts of interest.

Acknowledgments

This research is supported by the National Natural Science Foundation of China (Grant No. 51605390), Foundation of Educational Commission of Sichuan Province (Grant No. 16ZA0161), the Open Research Subject of Key Laboratory of Sichuan Provincial Automotive Engineering (Grant No. szjz2015-048), Foundation of the Science and Technology Research and Development Program of Sichuan Province (Grant No. 2017GZ0103).

References

- [1] M. Divandari and A. Dadpour, "Radial force and torque ripple optimization for acoustic noise reduction of SRM drives via fuzzy logic control," in *Proceedings of the 2010 9th IEEE/LAS International Conference on Industry Applications, INDUSCON 2010*, Brazil, November 2010.
- [2] F. L. dos Santos, J. Anthonis, and H. Van der Auweraer, "Multiphysics thermal and NVH modeling: Integrated simulation of a switched reluctance motor drivetrain for an electric vehicle," in *Proceedings of the 2012 IEEE International Electric Vehicle Conference (IEVC)*, pp. 1–7, Greenville, SC, USA, March 2012.
- [3] I. Husain, A. Radun, and J. Nairus, "Unbalanced force calculation in switched-reluctance machines," *IEEE Transactions on Magnetics*, vol. 36, pp. 330–338, 2000.
- [4] N. K. Sheth and K. R. Rajagopal, "Variations in overall developed torque of a switched reluctance motor with airgap nonuniformity," *IEEE Transactions on Magnetics*, vol. 41, no. 10, pp. 3973–3975, 2005.
- [5] B. M. Ebrahimi, J. Faiz, and M. J. Roshtkhari, "Static-, dynamic-, and mixed-eccentricity fault diagnoses in permanent-magnet synchronous motors," *IEEE Transactions on Industrial Electronics*, vol. 56, no. 11, pp. 4727–4739, 2009.
- [6] N. K. Sheth and K. R. Rajagopal, "Effects of nonuniform airgap on the torque characteristics of a switched reluctance motor," *IEEE Transactions on Magnetics*, vol. 40, no. 4, pp. 2032–2034, 2004.
- [7] E. Afjei and H. Torkaman, "Airgap eccentricity fault diagnosis in switched reluctance motor," in *Proceedings of the 1st Power Electronics and Drives, Systems and Technologies Conference, PEDSTC 2010*, pp. 290–294, Iran, February 2010.
- [8] M. C. Ta and C. Dufour, "Real-time simulation and control of reluctance motor drives for high speed operation with reduced torque ripple," in *Proceedings of the 37th Annual Conference of the IEEE Industrial Electronics Society, IECON 2011*, pp. 4176–4181, Australia, November 2011.
- [9] X. D. Xue, K. W. E. Cheng, T. W. Ng, and N. C. Cheung, "Multi-objective optimization design of in-wheel switched reluctance motors in electric vehicles," *IEEE Transactions on Industrial Electronics*, vol. 57, no. 9, pp. 2980–2987, 2010.
- [10] H. Chaozhi, "A Stator novel structure to decrease vibration of switched reluctance motor," *China Micro Motor*, vol. 45, no. 9, pp. 37–40, 2017.
- [11] X. Zhang, X. Wang, Y. Yang, and B. Wei, "Vibration reduction of a switched reluctance motor using new rotor tooth with slot on each side," *Zhongguo Dianji Gongcheng Xuebao/Proceedings of the Chinese Society of Electrical Engineering*, vol. 35, no. 6, pp. 1508–1515, 2015.
- [12] P. C. Desai, M. Krishnamurthy, N. Schofield, and A. Emadi, "Novel switched reluctance machine configuration with higher number of rotor poles than stator poles: Concept to implementation," *IEEE Transactions on Industrial Electronics*, vol. 57, no. 2, pp. 649–659, 2010.
- [13] J. Ye, B. Bilgin, and A. Emadi, "An extended-speed low-ripple torque control of switched reluctance motor drives," *IEEE Transactions on Power Electronics*, vol. 30, no. 3, pp. 1457–1470, 2015.
- [14] P. Song, M. Tomizuka, and C. Zong, "A novel integrated chassis controller for full drive-by-wire vehicles," *Vehicle System Dynamics*, vol. 53, no. 2, pp. 215–236, 2015.
- [15] S. Ko, J. Ko, S. Lee, J. Cheon, and H. Kim, "A study on the road friction coefficient estimation and motor torque control for an in-wheel electric vehicle," *Proceedings of the Institution of Mechanical Engineers, Part D: Journal of Automobile Engineering*, vol. 229, no. 5, pp. 611–623, 2015.
- [16] Y. Wang, P. Li, and G. Ren, "Electric vehicles with in-wheel switched reluctance motors: Coupling effects between road excitation and the unbalanced radial force," *Journal of Sound and Vibration*, vol. 372, pp. 69–81, 2016.
- [17] Y.-Y. Wang, Y.-N. Li, W. Sun, and L. Zheng, "Effect of the unbalanced vertical force of a switched reluctance motor on the stability and the comfort of an in-wheel motor electric vehicle," *Proceedings of the Institution of Mechanical Engineers, Part D: Journal of Automobile Engineering*, vol. 229, no. 12, pp. 1569–1584, 2015.
- [18] J. Lin, K. W. E. Cheng, Z. Zhang, and X. Xue, "Experimental investigation of in-wheel switched reluctance motor driving system for future electric vehicles," in *Proceedings of the 2009*

3rd International Conference on Power Electronics Systems and Applications, PESA 2009, China, May 2009.

- [19] A. Labak and N. C. Kar, "Outer rotor switched reluctance motor design for in-wheel drive of electric bus applications," in *Proceedings of the 2012 XXth International Conference on Electrical Machines (ICEM)*, pp. 418–423, Marseille, France, September 2012.
- [20] R. Krishnan, *Switched Reluctance Motor Drives-Modeling, Simulation, Analysis, Design and Applications*, CRC Press, Boca Raton, Florida, 2001.
- [21] E. Bakker, L. Nyborg, and H. B. Pacejka, "Tyre modelling for use in vehicle dynamics studies," *SAE Technical Papers*, Article ID 870421, pp. 1–15, 1987.
- [22] L. Chai and T. Sun, "The design of LQG controller for active suspension based on analytic hierarchy process," *Mathematical Problems in Engineering*, vol. 2010, Article ID 701951, 19 pages, 2010.
- [23] S.-A. Chen, F. Qiu, R. He, and S.-L. Lu, "Method for choosing weights in a suspension LQG control," *Journal of Vibration and Shock*, vol. 27, no. 2, pp. 65–68, 2008.
- [24] T. Xiao and Y. Shihua, "Method of comparison matrix consistency adjustment based on AHP," *Ordnance Industry Automation*, vol. 27, no. 4, 2008.



Hindawi

Submit your manuscripts at
www.hindawi.com

